



PERGAMON

International Journal of Impact Engineering 25 (2001) 869–886

INTERNATIONAL  
JOURNAL OF  
**IMPACT  
ENGINEERING**

www.elsevier.com/locate/ijimpeng

## Dynamic behavior of concrete at high strain rates and pressures: I. experimental characterization

D.L. Grote, S.W. Park<sup>1</sup>, M. Zhou\*

*The George W. Woodruff School of Mechanical Engineering, Georgia Institute of Technology, Atlanta,  
GA 30332-0405, USA*

Received 1 June 1999; received in revised form 16 October 1999; accepted 6 April 2001

### Abstract

Understanding the behavior of concrete and mortar at very high strain rates is of critical importance in a range of applications. Under highly dynamic conditions, the strain-rate dependence of material response and high levels of hydrostatic pressure cause the material behavior to be significantly different from what is observed under quasistatic conditions. The behavior of concrete and mortar at strain rates of the order of  $10^4 \text{ s}^{-1}$  and pressures up to 1.5 GPa are studied experimentally. The mortar analyzed has the same composition and processing conditions as the matrix phase in the concrete, allowing the effect of concrete microstructure to be delineated. The focus is on the effects of loading rate, hydrostatic pressure and microstructural heterogeneity on the load-carrying capacities of the materials. This experimental investigation uses split Hopkinson pressure bar (SHPB) and plate impact to achieve a range of loading rate and hydrostatic pressure. The SHPB experiments involve strain rates between 250 and  $1700 \text{ s}^{-1}$  without lateral confinement and the plate impact experiments subject the materials to deformation at strain rates of the order of  $10^4 \text{ s}^{-1}$  with confining pressures of 1–1.5 GPa. Experiments indicate that the load-carrying capacities of the concrete and mortar increase significantly with strain rate and hydrostatic pressure. The compressive flow stress of mortar at a strain rate of  $1700 \text{ s}^{-1}$  is approximately four times its quasistatic strength. Under the conditions of plate impact involving impact velocities of approximately  $330 \text{ ms}^{-1}$ , the average flow stress is 1.7 GPa for the concrete and 1.3 GPa for the mortar. In contrast, the corresponding unconfined quasistatic compressive strengths are only 30 and 46 MPa, respectively. Due to the composite microstructure of concrete, deformation and stresses are nonuniform in the specimens. The effects of material inhomogeneity on the measurements during the impact experiments are analyzed using a four-beam VISAR laser interferometer system. © 2001 Elsevier Science Ltd. All rights reserved.

**Keywords:** Concrete; Dynamic behavior; High strain rate; Hydrostatic pressure; Plate impact; Split Hopkinson pressure bar

\*Corresponding author. Tel.: +1-404-894-3294; fax: +1-404-894-0186.

E-mail address: min.zhou@me.gatech.edu (M. Zhou).

<sup>1</sup>Currently, US Federal Highway Administration, TFHRC/HRDI/PSI, 6300 Georgetown Pike, McLean, VA 22101.

### Nomenclature

$A$	cross-sectional area of the test specimen
$A_b$	cross-sectional area of the Hopkinson bars
$c$	longitudinal wave speed of the anvil plate material
$c_b$	longitudinal wave speed in the Hopkinson bar
$D$	diameter of the test specimen
$E_b$	Young's modulus of the Hopkinson bar material
$L$	length of the test specimen
$V_0$	projectile velocity in impact experiments
$V_{fs}$	velocity measured on the rear surface of the anvil plate
$\varepsilon$	longitudinal strain
$\dot{\varepsilon}$	longitudinal strain rate
$\varepsilon_R$	strain measured on the input Hopkinson bar
$\varepsilon_T$	strain measured on the output Hopkinson bar
$\rho$	mass density of anvil plate material
$\sigma$	longitudinal stress

## 1. Introduction

The response of concrete to dynamic loading is of interest in a variety of civilian and military applications. Understanding the response of concrete to impact or explosive loading is important for the successful destruction of military targets and for the effective protection of defense structures. For example, the protective shells of nuclear power plants are expected to survive the impact loading of an incoming missile or other sources. Airport runways must withstand repeated dynamic loads due to aircraft takeoff and landing. Dynamic loading on concrete structures arising from natural hazards such as tornadoes, earthquakes and ocean waves is also of great practical concern. Characterization of the behavior of concrete under impact or impulsive loading is a prerequisite for the design and analysis of these structures.

When concrete is subjected to dynamic loading of sufficient amplitude, fracture, fragmentation and pulverization occur. The entire process consists of initial elastic response, plastic flow, micro- and macro-crack formation, fragmentation, rubblization and flow of rubblized granules. In addition to initial strength, the comminution and post-rubblization flow also play a significant role in determining the response of concrete during impact. For example, the effectiveness of a blast or a penetrator depends strongly on the deformation, failure and the removal of materials from the front of the projectile because the flow of the granules occurs over a major portion of the entire process. Clearly, the load-carrying capacity and energy absorbency of the target materials undergo dramatic evolution throughout the process. This evolution plays an important role in determining the performance of structures and the effectiveness of penetrators. In order to establish models that can be used to simulate and predict the response of structures made of such materials, it is necessary to quantify experimentally their response to high rates of loading under various multiaxial states of stress and to characterize their behavior throughout the stages of deformation.

The mechanical behavior of concrete has been found to depend on strain rate over a wide range of conditions [1–19]. The range of strain rate studied is usually dictated by the type of loading devices employed. For instance, Bresler and Bertero [17] and Takeda and Tachikawa [18] used hydraulic testing machines to load specimens at strain rates up to  $1 \text{ s}^{-1}$ . Hughes and Gregory [14], Watstein [15] and Hughes and Watson [19] used a drop-weight impactor to achieve strain rates on the order of  $10 \text{ s}^{-1}$ . Ross et al. [1–3] and Malvern et al. [10] used a split Hopkinson pressure bar and obtained deformation rates of the order of  $10\text{--}10^3 \text{ s}^{-1}$ . These investigations concerned only strain rates under  $10^3 \text{ s}^{-1}$ . Furthermore, the conditions do not involve the high hydrostatic pressures that exist in impact and penetration. Partly because of the absence of hydrostatic pressure, these experiments simulate only the early stages of deformation and failure such as fracture and fragmentation but do not simulate the post-fracture processes of pulverization and granular flow. The rate dependence is stronger at higher strain rates. For example, the Hopkinson bar experiments of Ross et al. [1–3] showed that there is a sharp upturn in the strength of concrete in the strain rate region of  $10\text{--}10^3 \text{ s}^{-1}$ . Deformation and failure of concrete structures subjected to impact or penetration have also been studied [20–24]. Dancygier and Yankelevsky [25] and Dancygier [26] found that high strength concrete is much more effective in resisting impact loading than normal strength concrete. Kipp et al. [27] reported an average dynamic spall strength of 30 MPa at impact velocities of  $30\text{--}220 \text{ ms}^{-1}$  for two different concrete formulations. Kennedy [28] and Barr [29] have provided guidelines for the design and analysis of concrete structures accounting for enhanced dynamic failure resistance.

Two of the most important factors influencing the behavior of concrete under dynamic conditions are strain-rate sensitivity and pressure dependence. Despite the work reported, there is still a lack of data and understanding for conditions involving very high strain rates and high hydrostatic pressures. The currently available data concern only strain rates up to  $10^3 \text{ s}^{-1}$  and pressures up to several hundred MPa. In order to obtain realistic characterizations and develop constitutive models for the materials in applications such as impact, penetration and blast, experimental data for conditions beyond what has been analyzed are needed. This need motivated the current study. This study is aimed at producing data for the extreme conditions not yet fully simulated in laboratory or analyzed in modeling. The approach is to use plate impact and split Hopkinson bar experiments to generate strain rates over the range of  $10^2\text{--}10^4 \text{ s}^{-1}$  and pressures of up to 1.5 GPa. These conditions more closely simulate those found in actual penetration and explosion. For comparison purposes, quasistatic experiments are also conducted. Since the evolution of microstructure greatly changes the behavior of concrete as deformation progresses, the experiments emphasize time-resolved analysis of the changes in the load-carrying capacities of the materials. To this end, laser interferometry and high-speed digital oscilloscopes are used to obtain deformation and stress histories in the materials. The experimental data obtained are used to calibrate the constitutive model employed in numerical simulations presented in Park et al. [30]. Finite element simulations reported in the companion paper focus on the dynamic load-carrying and energy-absorbing capabilities of concrete under the conditions of the plate impact experiments discussed in this paper. The numerical simulations use a micro-mechanical model of the concrete microstructure and explicitly account for the arbitrary two-phase microstructural morphology of the concrete. The effects of individual phase properties, phase distributions and phase volume fraction on the dynamic behavior of concrete are quantitatively analyzed.

## 2. Materials

The materials analyzed are a G-mix concrete with the maximum aggregate size of 9.5 mm and a pure mortar. Both materials are provided by Tyndall Air Force Base and have the same processing conditions. The pure mortar also has the same composition as the mortar phase in the concrete. When tested separately, it provides a means for obtaining the response of the mortar phase in the concrete. It must be pointed out that the in situ properties of the mortar phase may not be exactly the same as those of the pure mortar, especially the degree of porosity in the matrix phase could be different from that of the pure mortar. However, a microscopic observation revealed that such difference in porosity is very small and insignificant. Cross sections of a mortar and a concrete specimen are shown in Fig. 1. The composition of the fly ash contained in the pure mortar and the mortar phase in the concrete is shown in Table 1. The proportions of the fly ash components meet the requirements of ASTM and AASHTO. The gradation of aggregate used in the concrete is given in Fig. 2. The volume fraction of the aggregate in the concrete is 42%. The Young's modulus, Poisson's ratio and density for both materials are listed in Table 2. The densities are directly measured. The Young's modulus and Poisson's ratio are determined through ultrasonic measurements of the wave speeds in the materials.

## 3. Quasistatic compression experiments

For comparison purposes, experiments are conducted to determine the quasistatic compressive strengths of concrete and mortar under conditions of uniaxial stress. Cylindrical specimens 3 in in diameter and 6 in in length are subjected to unconfined compression at a nominal strain rate of  $10^{-3} \text{ s}^{-1}$  following ASTM standard C39-96. The results of the experiments are summarized in Table 3. The quasistatic compressive strength of the mortar (approximately 46 MPa) is found to

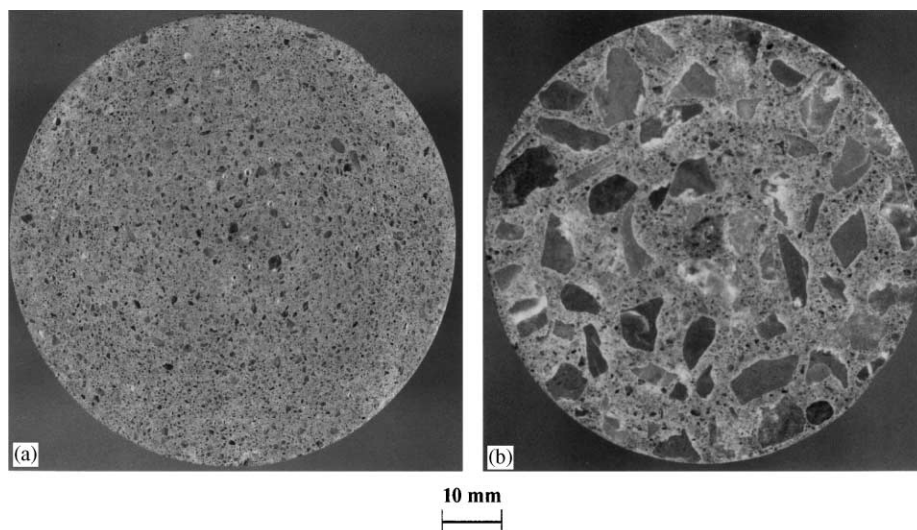


Fig. 1. Cross sections of specimens before experiment (diameter: 76.2 mm); (a) mortar, (b) concrete.

Table 1  
Composition of the fly ash used in mortar and concrete specimens

Components	Vol%	ASTM C618 spec. (class F)	AASHTO M295 spec. (class F)
Silicon dioxide ( $\text{SiO}_2$ )	50.7		
Aluminum oxide ( $\text{Al}_2\text{O}_3$ )	24.9		
Iron oxide ( $\text{Fe}_2\text{O}_3$ )	13.8		
Sum of $\text{SiO}_2$ , $\text{Al}_2\text{O}_3$ , $\text{Fe}_2\text{O}_3$	89.4	70.0% Min	70.0% Min
Calcium oxide ( $\text{CaO}$ )	3.1		30.0% Max
Magnesium oxide ( $\text{MgO}$ )	1		5.0% Max
Sulfur trioxide ( $\text{SO}_3$ )	0.5	5.0% Max	5.0% Max
Moisture content	0.2	3.0% Max	3.0% Max
Loss on ignition	3.6	6.0% Max	5.0% Max
Amount retained on No.325 sieve	22	34.0% Max	34.0% Max
Specific gravity	2.31		

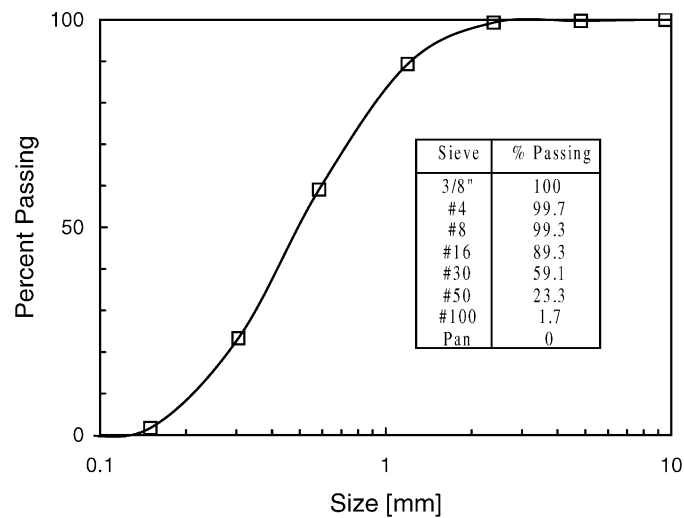


Fig. 2. Gradation of the aggregate used in the concrete specimens.

Table 2  
Material constants for mortar and aggregate

	Young's modulus (GPa)	Poisson's ratio	Density ( $\text{kg/m}^3$ )
Mortar	20	0.2	2100
Aggregate	45	0.29	2600

Table 3

Quasistatic compression tests on concrete and mortar

	Specimen #1	Specimen # 2	Specimen # 3
Material	Concrete	Mortar	Mortar
Specimen diameter (in)	3.0	3.0	3.0
Length (in)	6.0	6.0	6.0
Maximum load (kips)	30.5	46.0	48.5
Compressive strength (MPa)	29.7	44.8	47.3
Failure mode	Shear	Cone and shear	Cone and shear

be higher than that of the concrete (approximately 30 MPa). This difference in strength is related to different deformation and failure mechanisms in these materials. In concrete, microcracks readily develop and grow along the aggregate-matrix interfaces due to high stress concentrations at these interfaces and due to weak interfacial bonding [31,32]. These microcracks coalesce and develop into macrocracks under increased loading, leading to a premature failure of concrete compared to mortar. The quasistatic strengths provide a baseline level with which dynamic flow stress levels will be compared.

#### 4. Split Hopkinson pressure bar experiments

To obtain the dynamic stress-strain behavior of mortar at intermediate strain rates, a series of split Hopkinson pressure bar (SHPB) experiments are conducted. The specimens are circular cylinders 19.05 mm (or 12.70 mm) in diameter. Specimens with different aspect (length to diameter) ratios are used. The strain rates achieved range from 250 to  $1700 \text{ s}^{-1}$ . Details of each experiment including specimen dimensions and the resulting dynamic compressive strengths are listed in Table 4. The results are used in Park et al. [30] to formulate a constitutive model for the mortar phase in the concrete. Due to the coarse aggregate in the concrete and limitations on the specimen diameter that can be accommodated by the SHPB apparatus, no SHPB experiments are conducted on the concrete.

Fig. 3 is a schematic illustration of the SHPB apparatus used. The technique is based on the theory of one-dimensional wave propagation in an elastic bar. This split-bar configuration was developed by Kolsky [33] following the original introduction by Hopkinson [34] and a comprehensive study by Davies [35]. Over the years, the technique has been extended to tensile [36] and torsional [37] configurations.

The specimen is placed between the input and output bars. The striker bar, propelled by pressurized gas, impacts against the input bar. Upon impact, a compressive stress pulse is generated in the striker and input bar. The duration of the loading pulse is equal to the time for stress wave to traverse back and forth once in the striker bar. The compressive stress pulse then impinges on the specimen sandwiched between the input and output bars. Part of the incident pulse is reflected back into the input bar from the input bar/specimen interface and part of it is transmitted through the specimen into the output bar. A strain gage station

Table 4  
Split Hopkinson pressure bar experiments on mortar

Test ID	Strain rate ( $\text{s}^{-1}$ )	Compressive strength (MPa)	Specimen diameter, $D$ (mm)	Specimen length, $L$ (mm)	$L/D$	Diameter of pressure bar used (mm)
1	450	60	15.2	11.7	0.76	19.05
2	450	70	15.2	11.2	0.73	19.05
3	1000	110	10.1	5.5	0.54	19.05
4	700	65	10.1	10.5	1.04	12.70
5	480	60	10.8	16.0	1.48	12.70
6	500	60	10.8	15.2	1.41	12.70
7	650	65	11.3	14.2	1.27	12.70
8	1350	125	11.3	14.2	1.26	12.70
9	700	85	11.4	6.0	0.52	19.05
10	800	85	11.9	6.3	0.53	19.05
11	940	95	11.7	6.0	0.51	19.05
12	850	95	11.9	5.5	0.46	19.05
13	600	80	12.0	5.8	0.49	19.05
14	620	78	11.6	5.9	0.51	19.05
15	900	90	11.5	5.9	0.51	19.05
16	1350	110	11.4	4.8	0.42	19.05
17	400	55	11.8	11.4	0.97	19.05
18	290	50	11.9	11.7	0.99	19.05
19	700	65	11.9	11.9	1.00	19.05
20	300	45	12.1	17.7	1.47	19.05
21	350	60	11.5	17.8	1.55	19.05
22	280	40	12.3	17.3	1.4	19.05
23	400	70	12.0	12.3	1.03	19.05
24	1050	110	12.0	5.6	0.47	19.05
25	1500	160	11.2	5.5	0.49	19.05
26	1700	180	11.4	5.1	0.45	19.05
27	680	110	11.4	11.4	1.00	19.05
28	660	100	11.4	12.8	1.12	19.05
29	830	142	18.7	6.2	0.33	19.05
30	880	147	18.7	5.8	0.31	19.05
31	250	75	18.8	14.2	0.75	19.05

is placed on the input bar and another on the output bar. The strain gage output signals are recorded on a digital oscilloscope. Fig. 4(a) shows the signals recorded from the strain gages mounted on the input and output bars during an experiment. These strain measurements are used to determine the time histories of the stress, strain and strain rate in the specimen during deformation. Specifically, the stress and strain histories are [38], respectively,

$$\sigma(t) = E_b \frac{A_b}{A} \varepsilon_T(t) \quad (1)$$

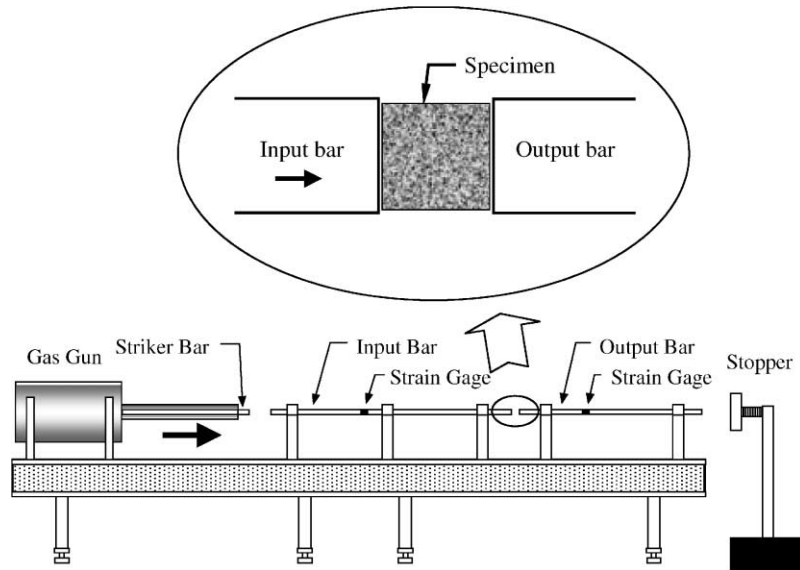


Fig. 3. A schematic illustration of the split Hopkinson pressure bar apparatus.

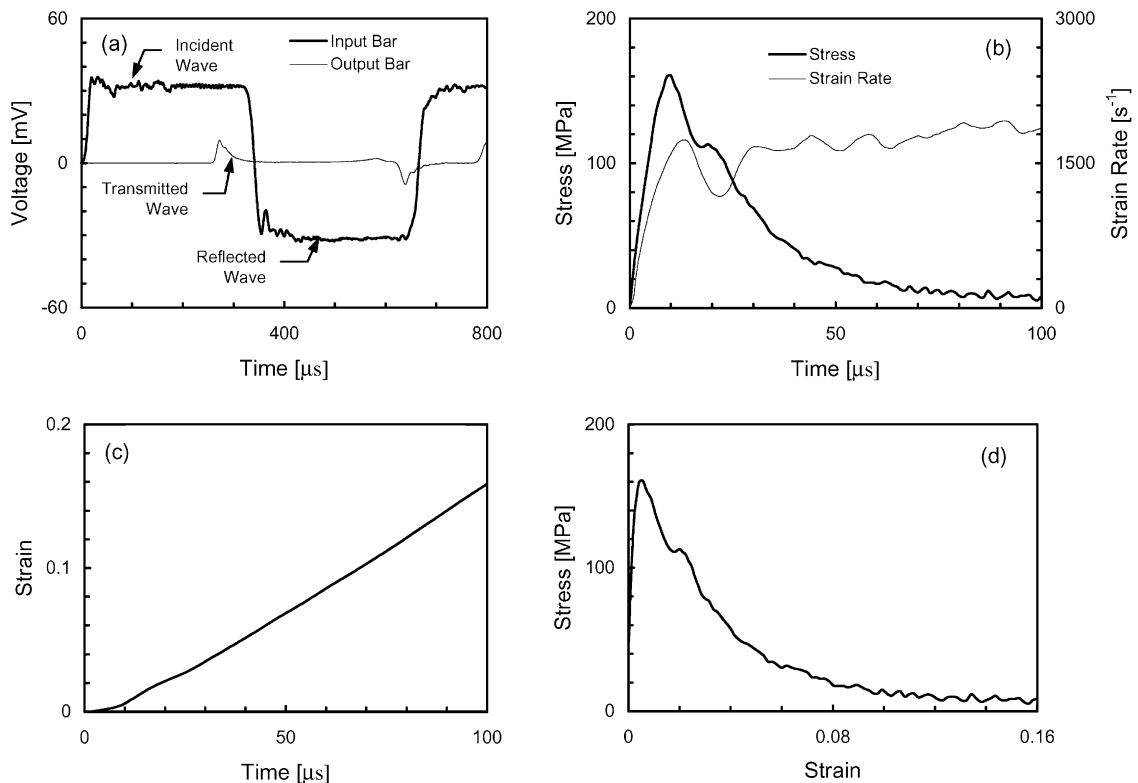


Fig. 4. Data analysis for an SHPB experiment; (a) measured strain gage signals, (b) computed stress and strain rate histories, (c) computed strain history, and (d) stress-strain relationship.



and

$$\dot{\varepsilon}(t) = \frac{-2c_b}{L} \varepsilon_R(t), \quad (2)$$

where  $\varepsilon_T$  and  $\varepsilon_R$  denote the amplitudes of the transmitted and reflected strain pulses.  $E_b$ ,  $A_b$  and  $c_b$  denote the Young's modulus, cross-sectional area and longitudinal wave speed of the bars, and  $A$  and  $L$  are the cross-sectional area and length of the specimen, respectively. The expression for the strain rate in (2) may be integrated with respect to time to give the strain, i.e.,

$$\varepsilon(t) = \frac{-2c_b}{L} \int_0^t \varepsilon_R(\tau) d\tau. \quad (3)$$

Fig. 4(b) shows the stress and strain rate histories obtained from the reflected and transmitted strain histories shown in Fig. 4(a). The strain rate is not constant throughout the period in general due to the dynamic nature of the experiment. An average strain rate is calculated and used for the duration of loading. The average strain rate for the test shown in Fig. 4 is  $1500 \text{ s}^{-1}$ . The strain history computed according to (3) is shown in Fig. 4(c). The history of stress in Fig. 4(b) and the history of strain in Fig. 4(c) combine to yield the stress-strain relation shown in Fig. 4(d).

In a SHPB test, the specimen must be short enough for a uniform state of stress along the length of the specimen to be rapidly achieved during loading. Five to ten wave reverberations within the specimen are normally required [39]. On the other hand, when very short specimens are used, friction between the specimen ends and the bars can play a significant role and lead to an apparent increase in strength [40]. The diameter of the specimen also needs to be small relative to the wavelength of the applied load pulse for the one-dimensional wave theory to be valid without the complication of Pochhammer-Chree radial oscillations. Accounting for these restrictions, specimens with length ( $L$ ) ranging from 4.8 to 18.8 mm and diameter ( $D$ ) ranging from 5.1 to 15.2 mm are used in the experiments. These specimens have aspect ratios ( $L/D$ ) between 0.31 and 1.55, see Table 4. Davies and Hunter [41] suggested that the optimum aspect ratio be  $L/D = \sqrt{\frac{3}{4}} \nu$ , where  $\nu$  is the Poisson's ratio of the specimen material. In most cases, this condition yields  $L/D \approx 0.5$ . In the experiments conducted here, aspect ratios between 0.31 and 1.55 are used to achieve a range of strain rates for the characterization of strain rate sensitivity. Multiple tests show that specimens with aspect ratios in this range yield consistent stress-strain curves for the same strain rate and no obvious size effect is observed.

The stress-strain curves of mortar at four different strain rates are shown in Fig. 5. Clearly, the compressive strength increases with increasing strain rate. At a strain rate of  $\dot{\varepsilon} = 1500 \text{ s}^{-1}$ , the compressive strength is 160 MPa or approximately 3.5 times the quasistatic strength. The curves indicate strain-softening after the peak stress, reflecting fragmentation and granular flow. The similar shapes of these stress-strain curves allow the strain-rate sensitivity of the flow stress to be characterized using a simple scaling function. This strain-rate dependence of the compressive strength is shown in Fig. 6. The dynamic strength values are normalized with respect to the quasistatic strength of 46 MPa. The symbols denote experimental points and the continuous line represents a curve fit of the data. Due to the lack of available experimental data between the quasistatic regime and the SHPB impact regime, the following straight-line fit is employed over this range of strain rate:

$$R = 0.0235 \log \dot{\varepsilon} + 1.07, \quad (4)$$

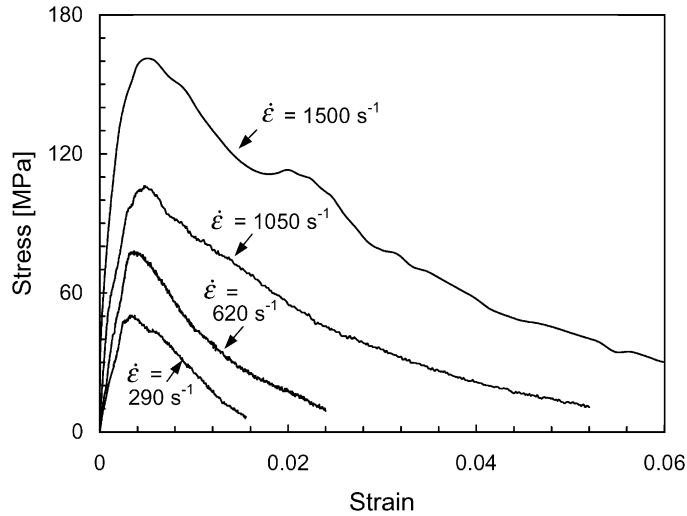


Fig. 5. Stress-strain behavior of mortar at different strain rates.

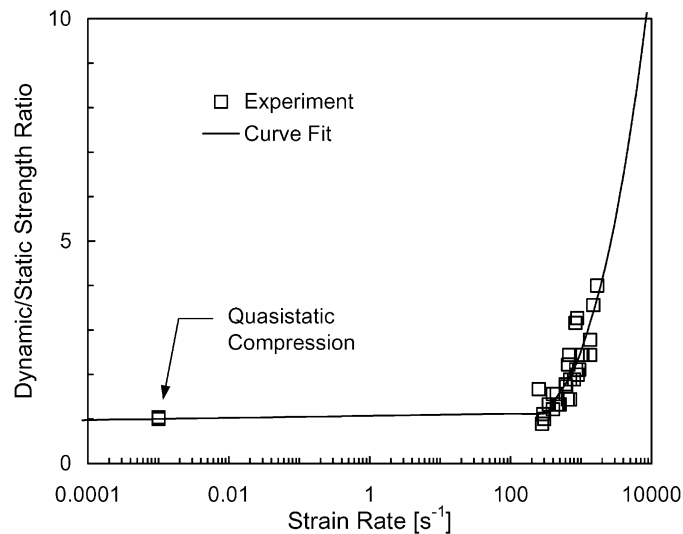


Fig. 6. Strain-rate dependence of the compressive strength of mortar (normalized with respect to the quasistatic strength).

where  $R$  is the ratio of dynamic to quasistatic flow stresses and  $\log \equiv \log_{10}$ . The nonlinear part of the curve is characterized by

$$R = 0.882(\log \dot{\epsilon})^3 - 4.48(\log \dot{\epsilon})^2 + 7.22(\log \dot{\epsilon}) - 2.64. \quad (5)$$

The SHPB tests cover strain rates between 250 and 1700  $\text{s}^{-1}$ . A sharp increase in dynamic strength is observed over the range of strain rates achieved by the SHPB experiments. This finding

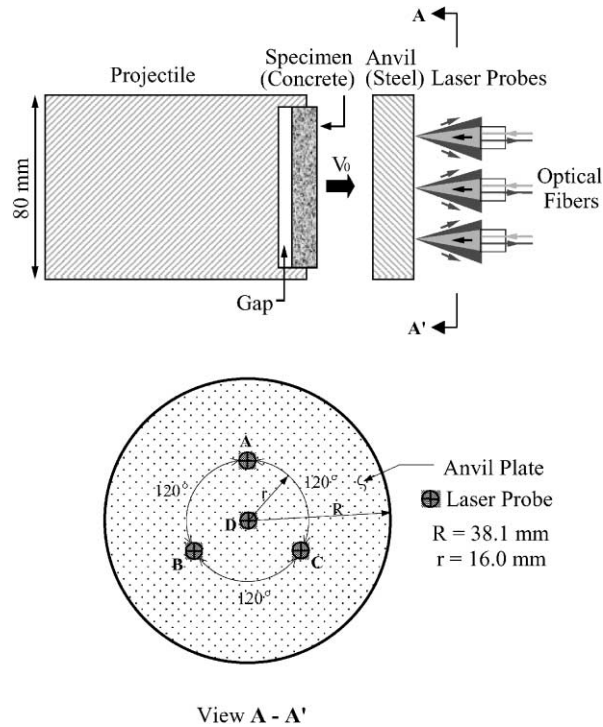


Fig. 7. Configuration of the plate impact experiment.

is consistent with the results reported by Ross and coworkers [2]. Different formulas have been proposed for the characterisation of the rate-sensitivity of the compressive strength of concrete. For example, CEB [42] suggested formulas for representing a slow increase in strength for strain rates up to  $30 \text{ s}^{-1}$  and a rapid increase for strain rates greater than  $30 \text{ s}^{-1}$ . Fig. 6 shows an extrapolated behavior beyond the strain rate of  $1700 \text{ s}^{-1}$ . This characterization is used in the numerical simulations discussed in Park et al. [30].

The strain at which the maximum compressive stress occurs is an important parameter in the characterization of material behavior. There have been differing reports as to how this strain varies with strain rate. Watstein [15], Takeda and Tachikawa [43], and Kvirikadze [44] have reported that this strain increases with increasing strain rate. On the other hand, Hatano and Tsutsumi [45], Cowell [46] found that it remains essentially constant while Hughes and Watson [19], Dilger et al. [47], and Dhir and Sangha [48] have reported that it decreases with strain rate. The contradictory findings can partly be attributed to the inconsistency among the methods of loading and associated errors. For example, Watstein [15] reported that the strain at maximum stress decreases with strain rate when tests are conducted using a hydraulic machine while it increases with strain rate when the specimens are loaded with a drop-hammer. Fig. 5 appears to indicate that the strain at maximum stress increases slightly with increasing strain rate. However, the amount of increase is very small and may well be within the range of experimental error. In the numerical simulations reported in Park et al. [30], this strain is assumed to remain constant at different strain rates.

## 5. Plate impact experiments

Plate impact provides a unique means to generate extremely high strain rates and high pressures under well-controlled conditions. In this study, normal impact experiments are conducted on circular disks of concrete and mortar to characterize their dynamic stress-carrying capacities. Average strain rates achieved are of the order of  $10^4 \text{ s}^{-1}$ . Since attention is focused on the time period before cylindrical unloading waves arrive at the center of the impacted specimen, the central region remains in a state of nominally uniaxial strain due to lateral inertial confinement. Confining pressures in the experiments conducted are of the order of 1–1.5 GPa.

A schematic illustration of the impact configuration is shown in Fig. 7. The specimens are 76.2 mm in diameter and 10 mm in thickness. The end surfaces are lapped flat and the actual thickness is within 0.0254 mm of 10 mm. The specimen is placed at the front of the projectile assembly. A gap between the disk specimen and the projectile tube is provided to allow a traction-free end condition for the back surface of the specimen during the impact process. The specimen impacts against an anvil plate made of hardened Hampden tool steel. The target steel is heat-treated to have a hardness of approximately 65 on the Rockwell C scale and has a thickness of 13.5 mm. The projectile is propelled by pressurized helium gas. The impact occurs in a vacuum chamber located at the muzzle end of a gas gun. The velocity of the projectile  $V_0$  is measured immediately prior to impact using wire pins.

Upon impact, compressive stress waves are generated in both the specimen and the anvil plate. These waves propagate from the impact face toward the rear surface of the specimen and the rear surface of the anvil plate. Upon arriving at the rear free surfaces, these compressive waves are reflected as tensile waves. The reflected tensile waves then interfere destructively with the on-going incident compressive waves, reducing the compressive stresses in the specimen. The normal particle velocities at four points on the rear surface of the anvil plate are measured using a VISAR (Velocity Interferometer System for Any Reflector) laser interferometer system with an accuracy of  $\pm 2 \text{ ms}^{-1}$ . The four simultaneous measurements are made using four independent laser probes arranged as shown in Fig. 7. One probe (D) is focused at the center and the other three (A, B, and C) are focused on three points on a circle around the center. The latter probes are evenly spaced on the circle and are at a distance of 16 mm from the specimen center. The simultaneous measurements of velocities at different locations provide an opportunity for analyzing the heterogeneous deformation in the specimen. The interference signals from the laser interferometers are detected by photodiodes and recorded on a Tektronix TDS 784A digital oscilloscope with sampling rates of up to 4 billion samples per second.

The time-distance diagram shown in Fig. 8 indicates schematically how the waves propagate in the concrete specimen and the steel anvil plate during the impact process. The diagram is based on the one-dimensional wave propagation theory and the lines represent the longitudinal wave fronts at a given position and time. The construction of this diagram assumes that the materials involved are homogeneous and linearly elastic. This assumption does not consider the significant inelastic deformation and the material heterogeneity in the specimen. Therefore, this illustration should be viewed as an approximate representation for various wave fronts and a guide for experiment design. This diagram is also useful for the analysis and interpretation of experimental results. In addition to the nominally planar wave fronts, a cylindrical release wave also develops in the specimen and the target plate. This wave originates from the periphery at the impact face and

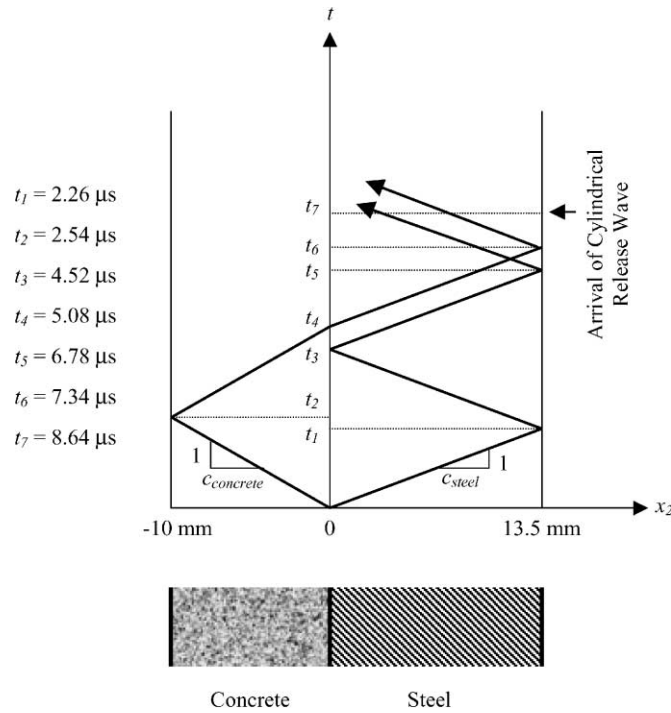


Fig. 8. Time-distance diagram for the plate impact experiment based on linear elastic material behavior.

propagates toward the center of the plates. This wave disrupts the well-characterized and nominally one-dimensional nature of the loading waves. In the analysis and discussion, attention is focused on the part of the experiment before this unloading wave arrives at the rear surface of the target plate ( $t_7$ ). The useful window for data analysis for the velocity profiles recorded on the rear surface is therefore  $t_7 - t_1$  which is approximately  $6.38 \mu\text{s}$  for the experimental configuration used.

The experiment is designed such that the target steel plate remains elastic throughout the impact process. Although the stress and velocity at the impact face are not uniform due to the inhomogeneous specimen properties, elastic wave propagation in the target plate allows the stress and velocity to become more uniform as they approach the rear surface of the target plate. This wave propagation process can be used as a mechanism for obtaining an average measure for the stress history at the impact face. According to the one-dimensional elastic wave theory, this average stress is related to the free surface particle velocity through [49].

$$\sigma(t) = \frac{1}{2} \rho c V_{fs}(t), \quad (6)$$

where  $\sigma$ ,  $V_{fs}$ ,  $\rho$  and  $c$  are, respectively, the average longitudinal stress at the specimen/target interface, particle velocity at the rear surface of the target, mass density and longitudinal wave speed of the anvil material. Eq. (6) allows the history of the longitudinal stress carried by the specimen to be inferred from the velocity history measured at the rear surface of the anvil plate.

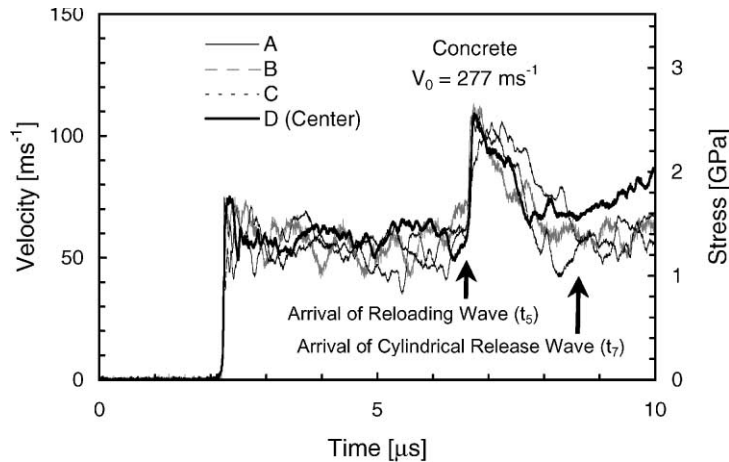


Fig. 9. Velocity profiles measured at different locations on the rear surface of the anvil plate (see Fig. 7 for probe locations) and the corresponding average stress in the concrete specimen interpreted according to (6).

Impact experiments conducted on mortar and concrete involve projectile velocities between 277 and  $330 \text{ ms}^{-1}$ . First, the effect of material heterogeneity on the velocity measurement is analyzed. Fig. 9 shows the free surface velocity histories measured at four different locations (as indicated in Fig. 7) on the rear surface of the anvil plate during an impact experiment on concrete. The impact velocity is  $277 \text{ ms}^{-1}$ . The corresponding average stresses interpreted from (6) are shown on the secondary vertical axis. The profiles show that the velocity begins to increase when the compressive wave arrives at the rear surface of the anvil plate at approximately  $2.2 \mu\text{s}$  after impact. The average value of the free surface velocity remains essentially constant until the wave reflected from the specimen/anvil interface arrives at the free surface of the anvil plate. The sudden increase in velocity at  $t \cong 6.8 \mu\text{s}$  coincides with  $t_5$  in Fig. 8. The four independent measurements show variations from each other. While the oscillations are not coordinated, the average values for the duration of interest between  $t_1$  ( $2.2 \mu\text{s}$ ) and  $t_5$  ( $6.8 \mu\text{s}$ ) are quite consistent. Specifically, the average velocity before the arrival of the reloading wave is approximately  $58 \text{ ms}^{-1}$  and the corresponding average stress is approximately 1.2 GPa. Furthermore, the level of oscillation is the same for all four profiles or approximately  $20 \text{ ms}^{-1}$  in terms of the velocity. It appears that any of the four curves can appropriately represent the response of the specimen, as long as the focus is on the average stress and the associated oscillation is accepted. The growing deviation of the center profile from the off-center profiles beginning at  $8.7 \mu\text{s}$  coincides with the arrival of the cylindrical unloading wave at the outer probes ( $t_7$  in Fig. 8). The part of the profiles beyond  $t_5$  ( $6.8 \mu\text{s}$ ) is not used to make interpretations concerning the load-carrying capacities of the specimen materials.

Based on the results of Fig. 9, the velocity profiles at the center of specimens are used to analyze the load-carrying capacities of concrete and mortar at different impact velocities. The profiles from two experiments with the same impact velocity of  $V_0 = 290 \text{ ms}^{-1}$ , one on mortar and the other on concrete, are shown in Fig. 10(a). The results of two other experiments with an impact velocity of  $V_0 = 330 \text{ ms}^{-1}$  are shown in Fig. 10(b). The profiles for the concrete exhibit more pronounced oscillations than those for mortar, reflecting the higher level of material heterogeneity

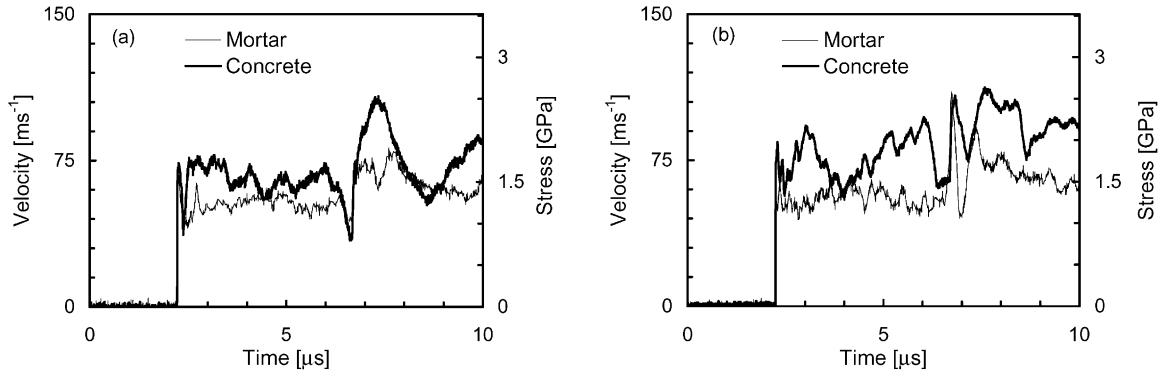


Fig. 10. Velocity profiles measured at the center of the rear surface of the anvil plate and the corresponding average stress in the mortar and concrete specimens interpreted according to (6); (a)  $V_0 = 290 \text{ ms}^{-1}$ , (b)  $V_0 = 330 \text{ ms}^{-1}$ .

in concrete. For mortar, the average stress for  $V_0 = 290$  and  $330 \text{ ms}^{-1}$  is 1.2 and 1.3 GPa, respectively. In contrast, the average stress carried by concrete is approximately 1.55 GPa for  $V_0 = 290 \text{ ms}^{-1}$  and 1.7 GPa for  $V_0 = 330 \text{ ms}^{-1}$ . Note that the strength of the mortar is approximately 46 MPa under the condition of quasistatic, uniaxial stress (see Table 3). The stress levels here are also at least 8 times those observed in Hopkinson bar experiments, (see Fig. 5). The marked increase in stress-carrying capacity is attributed to the effects of the high strain rates (on the order of  $10^4 \text{ s}^{-1}$ ) and the high lateral confining pressures (over 1 GPa). Based on the rate sensitivity characterization for mortar in Fig. 6 and (5) and using an average strain rate of  $10^4 \text{ s}^{-1}$ , approximately 42% of the strength increase (504 MPa) is attributed to strain rate dependence and 58% (696 MPa) is attributed to pressure sensitivity.

In quasistatic, uniaxial loading, the strength of concrete (30 MPa) is lower than that of mortar (46 MPa), as discussed earlier. Under the conditions of the impact experiment, the stress carried by the concrete is approximately 30% higher than that carried by the mortar. The differing results are due to different deformation and failure mechanisms associated with the quasistatic and dynamic experiments. Under uniaxial compression, the interfaces between the aggregate and matrix in concrete provide enhanced opportunities for crack initiation and growth, thus lowering its strength compared to pure mortar. Under the impact conditions, however, the high confining stresses tend to keep the interfaces under overall compressive loading, retarding the initiation and growth of cracks. The closure effect of the high hydrostatic stresses causes deformation to occur in both the mortar phase and the aggregate in concrete, allowing the strengthening effect of the aggregate to manifest. Consequently, the overall strength of concrete appears to be higher than that of mortar.

## 6. Conclusions

An experimental characterization of the dynamic behavior of concrete and mortar at very high strain rates and under high hydrostatic pressures is presented. Quasistatic compression, split

Hopkinson pressure bar and plate impact experiments are used, involving strain rates from  $10^{-3}$  to  $10^4 \text{ s}^{-1}$  and confining pressures from 0 to 1.5 GPa.

Experiments show that the behavior of mortar is significantly rate-sensitive in the strain-rate range of  $10^{-3}$ – $1700 \text{ s}^{-1}$ . The rate dependence is weaker for strain rates below  $400 \text{ s}^{-1}$ . Significantly stronger rate dependence is observed for strain rates above this transition rate. The experiments also show that the shape of the stress-strain curves at different rates are similar to each other and allow the strain-softening behavior of mortar to be characterized using a simple scaling function.

Under the conditions of plate impact, significantly higher stresses are carried by concrete and mortar than what is observed for the materials under conditions of quasistatic, uniaxial compression. The average flow stress of 1.7 GPa for the concrete and 1.3 GPa for the mortar was observed during experiments at an impact velocity of  $330 \text{ ms}^{-1}$  inducing strain rates on the order of  $10^4 \text{ s}^{-1}$  and hydrostatic pressures over 1 GPa. The marked increases in stress-carrying capacities under plate impact conditions are attributed to the effects of strain-rate hardening and the strong pressure-dependence of the response of the materials. Based on the results of quasistatic uniaxial compression and plate impact experiments on mortar, approximately 42% of the strength enhancement is due to rate sensitivity and 58% is attributed to the effect of hydrostatic pressure.

The average stress carried by concrete in plate impact experiments is approximately 30% higher than that of mortar, indicating the hardening effects of aggregate in concrete under impact loading. In contrast, the strength of concrete is found to be lower than that of pure mortar under conditions of quasistatic, uniaxial stress. The differing trends reflect the effects of different deformation and failure mechanisms in concrete under the quasistatic and impact loading. The key is the presence or lack of hydrostatic pressure. Under conditions of uniaxial stress, the interfaces between the aggregate and mortar in concrete provide enhanced opportunities for crack initiation and growth, limiting the strength of the overall composite. Under the conditions of the impact experiments, the closure effect of attendant hydrostatic pressure cause deformation to occur in the aggregate as well as in the mortar matrix, allowing the aggregate to act as reinforcement without inducing early failure in the form of interphase crack development.

Due to the material heterogeneity inherent in the concrete and mortar specimens, the stress and deformation are nonuniform in general. The plate impact configuration used provides a means with which an average measure for the stress carried by the materials under dynamic conditions can be obtained experimentally. Experiments show that point measurements taken on the rear surface of the target plate are individually indicative of the average stress history in the specimens analyzed.

The data obtained herein allows a constitutive relation for the response of concrete and mortar to be formulated for the strain rate regime of  $10^{-3}$ – $10^4 \text{ s}^{-1}$  and the pressure regime of 0–1.5 GPa. This relation is discussed and used by Park et al. [30] as part of a micromechanical model describing the dynamic behavior of concrete. A series of fully dynamic finite element simulations are carried out there to outline the effects of microstructure and phase volume fractions on the overall response.

## **Acknowledgements**

This research is sponsored by the US Air Force Office of Scientific Research under grants F49620-97-10055, F49620-97-1-0415 and F08671-98009587. We would like to thank Dr. J. Porter



at the Tyndall AFB for providing the materials used in the experiments. We would also like to thank Prof. L. L. Jacobs at Georgia Tech for performing the ultrasonic wave speed measurements on the materials.

## References

- [1] Ross CA, Thompson PY, Tedesco JW. Split-Hopkinson pressure-bar tests on concrete and mortar in tension and compression. *ACI Mater J* 1989;86(5):475–81.
- [2] Ross CA, Tedesco JW, Kuennen ST. Effects of strain rate on concrete strength. *ACI Mater J* 1995;92(1):37–47.
- [3] Ross CA, Jerome DM, Tedesco JW, Hughes ML. Moisture and strain rate effects on concrete strength. *ACI Mater J* 1996;94:293–300.
- [4] Tedesco JW, Ross CA, Kuennen ST. Experimental and numerical analysis of high-strain rate splitting-tensile tests. *ACI Mater J* 1993;90:162–9.
- [5] Bazant ZP, Gu WH, Faber KT. Softening reversal and other effects of a change in loading rate on fracture of concrete. *ACI Mater J* 1995;92(1):3–9.
- [6] Yon JH, Hawkins NM, Kobayashi AS. Strain-rate sensitivity of concrete mechanical properties. *ACI Mater J* 1992;89(2):146–53.
- [7] Takeda J-I. Strain rate effects on concrete and reinforcements, and their contributions to structures: In: Mindess S, Shah SP, editors. *Cement-based composites: strain rate effects on fracture*. Pittsburgh, PA, Materials Research Society, 1985. p. 15–20.
- [8] Shah SP. Concrete and fiber reinforced concrete subject to impact loading. In: Mindess S, Shah SP, editors. *Cement-based composites: strain rate effects on fracture*. Materials Research Society, 1985. p. 181–201.
- [9] Soroushian P, Choi K-B, Fu G. Tensile strength of concrete at different strain rates. In: Mindess S, Shah SP, editors. *Cement-based composites: strain rate effects on fracture*. Materials Research Society, 1985. p. 87–92.
- [10] Malvern LE, Jenkins DA, Tang T, Ross CA. Dynamic compressive testing of concrete. *Proceedings of Second Symposium on the Interaction of Non-Nuclear Munitions with Structures*. Florida: U.S. Dept. of Defense, 1985. p. 194–9.
- [11] Bischoff PH, Perry SH. Compressive strain rate effects of concrete. In: Mindess S, Shah SP, editors. *Cement-based composites: strain rate effects on fracture*. Materials Research Society, 1985. p. 151–65.
- [12] Bischoff PH, Perry SH. Compressive behaviour of concrete at high strain rates. *RIELM Mater Struct* 1991;24:425–50.
- [13] John R, Shah SP. Effects of high strength and rate of loading on fracture parameters of concrete. *Proceedings of SEM-RILEM International Conference Fracture. Concrete and Rock*, 1987. p. 35–52.
- [14] Hughes BP, Gregory R. Concrete subjected to high rates of loading in compression. *Mag Concr Res* 1972;24(78):25–36.
- [15] Watstein D. Effect of straining rate on the compressive strength and elastic properties of concrete. *ACI J* 1953;49(8):729–44.
- [16] Oh BH. Behavior of concrete under dynamic tensile loads. *ACI Mater J* 1987;84:8–13.
- [17] Bresler B, Bertero VV. Influence of high strain rate and cyclic loading of unconfined and confined concrete in compression. *Proceedings of Second Canadian Conference on Earthquake Engineering*. Hamilton, Ontario, 1975. p. 1–13.
- [18] Takeda J, Tachikawa H. The mechanical properties of several kinds of concrete at compressive, tensile, and flexural tests in high rates of loading. *Trans Architect Inst Jpn* 1962;77:1–6.
- [19] Hughes BP, Watson AJ. Compressive strength and ultimate strain of concrete under impact loading. *Mag Concr Res* 1978;30(105):189–99.
- [20] Chang WS. Impact of solid missiles on concrete barriers. *ASCE J Struct Div* 1981;107(2):257.
- [21] Haldar A, Hamieh H. Local effects of solid missiles on concrete structures. *ASCE J Struct Div* 1984;110(5):948.
- [22] Nickell RE, Rashid YR, Kurkchubasche IR. Low-velocity impact of missiles on reinforced concrete structures. *J Pressure Vessel Technol* 1991;113:127–32.

- [23] Shirai K, Ito C, Onuma H. Numerical studies of impact on reinforced concrete beam of hard missile. *Nucl Eng Des* 1994;150:483–9.
- [24] Yankelevsky DZ. Local response of concrete slabs to low velocity missile impact. *Int J Impact Eng* 1997;19(4):331–43.
- [25] Dancygier AN, Yankelevsky DZ. High strength concrete response to hard projectile impact. *Int J Impact Eng* 1996;18(6):583–99.
- [26] Dancygier AN. Rear face damage of normal and high-strength concrete elements caused by hard projectile impact. *ACI Struct J* 1998;95(3):291–304.
- [27] Kipp ME, Chhabildas LC, Reinhart WD. Elastic shock response and spall strength of concrete. In: Schmidt SC, Dandekar DP, Forbes JW, editors. *Proceedings of Tenth American Physical Society Topical Conference on Shock Compression of Condensed Matter*. Amherst, Massachusetts, July 27–August 1, 1997. p. 557–60.
- [28] Kennedy RP. A review of procedures for the analysis and design of concrete structures to resist missile impact effects. *Nucl Eng Des* 1976;37:183–203.
- [29] Barr P. *Guidelines for the design, assessment of concrete structures subjected to impact*. London: UK Atomic Energy Authority, HMSO, 1990.
- [30] Park SW, Xia Q, Zhou M. Dynamic behavior of concrete at high strain rates and pressures: part II. Numerical simulation. *Int. J. Impact Eng* 2001;25(9):887–910.
- [31] Chen W-F, Saleeb AF. *Constitutive equations for engineering materials*. New York: Wiley, 1982.
- [32] Shah SP, Swartz SE, Ouyang C. *Fracture mechanics of concrete*. New York: Wiley, 1995.
- [33] Kolsky H. An investigation of the mechanical properties of materials at very high rates of loading. *Proc Phys Soc* 1949;B62:676–700.
- [34] Hopkinson B. A method of measuring the pressure in the deformation of high explosives or by the impact of bullets. *Philos Trans R Soc* 1914;A213:437–52.
- [35] Davies RM. A critical study of the Hopkinson pressure bar. *Philos Trans R Soc London* 1948;A240:375–457.
- [36] Harding J, Wood ED, Campbell JD. Tensile testing of material at impact rates of strain. *J Mech Eng Sci* 1960;2:88–96.
- [37] Baker WW, Yew CH. Strain rate effects in the propagation of torsional plastic waves. *J Appl Mech* 1966;33:917–23.
- [38] Lindholm US. Some experiments with the split Hopkinson pressure bar. *J Mech Phys Solids* 1964;12:317–35.
- [39] Lindholm US. High strain rate tests. In: Bunshah RF, editor. *Measurement of mechanical properties*, vol. V, Part 1. New York: Interscience, 1971. p. 199.
- [40] Bertholf LD, Karnes CH. Two-dimensional analysis of the split Hopkinson pressure bar system. *J Mech Phys Solids* 1975;23(1):1–19.
- [41] Davies EDH, Hunter SC. The dynamic compression testing of solids by the method of the split Hopkinson pressure bar. *J Mech Phys Solids* 1963;11:155.
- [42] CEB., *Concrete structures under impact and impulsive loading*. Bulletin d'Information No. 187, Comité Euro-International du Béton, Lausanne, France, 1988.
- [43] Takeda J, Tachikawa H. Deformation and fracture of concrete subjected to dynamic load. *Proceedings of International Conference on Mechanical Behavior of Materials*. Kyoto, Japan, 1971. p. 267–77.
- [44] Kvirikadze OP. Determination of the ultimate strength and modulus of deformation of concrete at different rates of loading. *Proceedings of RILEM International Symposium on Testing In-Situ Concrete Structures*. Budapest, 1977. p. 109–17.
- [45] Hatano T, Tsutsumi H. Dynamical compressive deformation and failure of concrete under earthquake load. *Proceedings of Second World Conference on Earthquake Engineering*. Tokyo: Science Council of Japan, 1960. p. 1963–78.
- [46] Cowell WL. *Dynamic properties of plain Portland cement concrete*, Technical Report No. R447, US Naval Civil Engineering Laboratory, Port Hueneme, CA, 1966.
- [47] Dilger WH, Koch R, Kowalczyk R. Ductility of plain and confined concrete under different strain rates. *ACI J* 1984;81(1):73–81.
- [48] Dhir RK, Sangha CM. Study of the relationships between time, strength, deformation and fracture of plain concrete. *Mag Concr Res* 1972;24(81):197–208.
- [49] Clifton RJ, Klopp RW. Pressure-shear plate impact testing. In: Boyer HE, Gall TL, editors. *Metal's handbook*. 9th ed., vol. 8. Metals Park: American Society of Metals, 1985. p. 230–9.